mater.scichina.com link.springer.com

Published online 12 April 2022 | https://doi.org/10.1007/s40843-021-2006-y
Sci China Mater 2022, 65(9): 2401–2411

Hierarchically nitrogen-doped mesoporous carbon nanospheres with dual ion adsorption capability for superior rate and ultra-stable zinc ion hybrid supercapacitors

Zhongyou Peng[1], Junxi Guo[3], Qichang He[1], Shulong Li[1], Licheng Tan[1*] and Yiwang Chen[1,2*]

ABSTRACT **Although significant progress has been achieved in developing high energy aqueous zinc ion hybrid supercapacitors (ZHSCs), the sluggish diffusion of zinc ion (Zn^{2+}) and unsatisfactory cathodes still hinder their energy density and cycling life span. This work demonstrates the use of nitrogen-doped mesoporous carbon nanospheres (NMCSs) with appropriately hierarchical pore distribution and enhanced zinc ion storage capability for efficient Zn^{2+} storage. The as-prepared aqueous ZHSC delivers a significant specific capacity of 157.8 mA h g^{-1}, a maximum energy density of 126.2 W h kg^{-1} at 0.2 A g^{-1}, and an ultra-high power density of 39.9 kW kg^{-1} with a quick charge time of 5.5 s. Furthermore, the ZHSC demonstrates an ultra-long cycling life span of 50,000 cycles with an exciting capacity retention of 96.2%. More interestingly, a new type of planar ZHSC is fabricated with outstanding low-temperature electrochemical performance, landmark volumetric energy density of 31.6 mW h cm^{-3}, and excellent serial and parallel integration. Mechanism investigation verifies that the superior electrochemical capability is due to the synergistic effect of cation and anion adsorption, as well as the reversible chemical adsorption of NMCSs. This work provides not only an innovative strategy to construct and develop novel high-performance ZHSCs, but also a deeper understanding of the electrochemical characteristics of ZHSCs.**

Keywords: mesoporous carbon nanospheres, nitrogen doping, dual ion adsorption, anti-freezing electrolyte, zinc ion hybrid supercapacitors

INTRODUCTION

The rapid development of economic society and technology nowadays urgently requires efficient electrochemical energy storage (EES) devices with high energy density, high power density, long cycle life, and excellent safety [1–3]. Currently, various EES devices such as lithium ion batteries (LIBs), metal ion batteries, and supercapacitors (SCs) are being developed and employed in the electronics market. However, the large-scale applications of LIBs are hindered by unsatisfactory power density, poor cycle life, limited lithium resources, and inevitable safety issues [4,5]. Moreover, commercial lead-acid and nickel-based rechargeable batteries have a low energy density and limited life span, thereby resulting in high energy storage costs, which limits their practical applications. SCs characterized by fast charge/discharge rate, ultra-high power density, outstanding cycling stability, and superior safety are now regarded as one of the most competitive candidates to complement or replace batteries for energy storage. However, their inadequate energy density restricts their practical applications [6–8]. Therefore, developing safe and high energy density EES without sacrificing their power output and cycling lifetime by using less expensive aqueous electrolytes remains a formidable challenge.

Recently, zinc metal with a high theoretical capacity of 820 mA h g^{-1} (5851 mA h cm^{-3}), low redox potential of −0.76 V (*versus* standard hydrogen electrode (SHE)), and long operation lifetime [9,10] has been considered an ideal anode for aqueous zinc-based rechargeable batteries and capacitors. Nevertheless, zinc ion batteries based on transition metal oxide cathodes have an unsatisfactory rate capability and deficient cycling stability and/or specific capacity because of the dissolution and parasitic reactions, which lower the rate performance and cycle life [11–13]. Alternatively, aqueous Zn^{2+} hybrid SCs (ZHSCs), which usually constitutes a battery-type Zn anode and an electric double-layer capacitance (EDLC) carbon cathode in Zn^{2+} aqueous electrolyte, are expected to be a competitive power storage candidate, because it theoretically combines the advantages of battery and SC. The rapid exfoliating and depositing process of Zn^{2+} on Zn anode provides overall energy density, while the superb invertible adsorption/desorption of Zn^{2+} on the carbon cathode affords high power density and good cycling stability [14–18]. These extraordinary characteristics have prompted notable efforts to develop aqueous ZHSCs integrated with Zn anode and carbon cathode. For example, Kang's group [5] assembled a ZHSC that utilizes activated carbon (AC) as cathode with a high capacity of 121 mA h g^{-1} at 0.1 A g^{-1}, a high energy density of 84 W h kg^{-1}, and a power density of 14.9 kW kg^{-1}. Liu's group [12] used a porous carbon cathode to prepare ZHSCs, which presents a specific capacity of 132.7 mA h g^{-1}, a maximum energy density of 82.36 W h kg^{-1}, and a power den-

[1] College of Chemistry and Chemical Engineering/Institute of Polymers and Energy Chemistry (IPEC), Nanchang University, Nanchang 330031, China
[2] Institute of Advanced Scientific Research (iASR)/Key Lab of Fluorine and Silicon for Energy Materials and Chemistry of Ministry of Education, Jiangxi Normal University, Nanchang 330022, China
[3] School of Future Technology, Nanchang University, Nanchang 330031, China
[*] Corresponding authors (emails: tanlicheng@ncu.edu.cn (Tan L); ywchen@ncu.edu.cn (Chen Y))

sity of 3.76 kW kg^{-1}. In addition, heteroatom doping has been demonstrated to boost the charge storage capacity. Alshareef's group [19] assembled a ZHSC with an oxygen-rich porous carbon cathode, which delivers a specific capacity of 179.8 mA h g^{-1} and a high energy density of 104.8 W h kg^{-1}. Recently, Lu's group [20] reported that ZHSCs based on nitrogen-doped porous carbon cathode exhibit a high energy density of 107.3 W h kg^{-1} and a superb power density of 24.9 kW kg^{-1}. Yet, the unsatisfactory energy density and cycling life span of the currently reported ZHSCs restrict their practical applications due to the inappropriate pore distribution and the intrinsically insufficient capacity of corresponding carbonic cathodes, especially at a high current density and high mass loading. Moreover, the EES mechanism of ZHSCs has not yet been revealed.

In this work, hierarchically nitrogen-doped mesoporous carbon nanospheres (NMCSs) are synthesized for efficient ZHSCs. Hierarchically mesoporous nanostructure not only offers ample active sites for Zn^{2+} storage but also ensures consecutive electron transport and ion diffusion pathways. Moreover, nitrogen doping contributes to the chemical adsorption process of Zn^{2+} onto the cathode surface. As a result, the as-assembled aqueous ZHSCs based on NMCS cathode and Zn anode deliver a remarkable capacity (157.8 mA h g^{-1} at 0.2 A g^{-1}), a high energy density of 126.2 W h kg^{-1}, an ultra-high power density of 39.9 kW kg^{-1}, and an ultra-long cycling life (96.2% capacity retention after 50,000 cycles). An anti-freezing (AF) planar asymmetric ZHSC is demonstrated to have ultra-high volumetric energy density (31.6 mW h cm^{-3}), long-term durability, and efficient serial and parallel integration. Furthermore, to reveal the energy storage mechanism and understand the electrochemistry of ZHSCs, *ex-situ* X-ray diffraction (XRD), X-ray photoelectron spectroscopy (XPS), scanning electron microscopy (SEM), and *in-situ* electrochemical quartz crystal microbalance (EQCM) experiments verify that the superior electrochemical capability is due to the synergistic effect of cation and anion adsorption, as well as the reversible chemical adsorption of NMCSs during charge/discharge processes.

EXPERIMENTAL SECTION

Chemicals and materials

All the reagents and solvents, unless otherwise stated, were obtained from commercial sources (Sigma Aldrich, Alfa Aesar, and Sinopharm Chemical Reagent Co., Ltd. Shanghai, China) and were used without further purification.

Synthesis of NMCSs

NMCSs were synthesized by performing a two-step process. First, 5.2 mL of tetrapropyl orthosilicate was added to the mixed solution, including 105 mL of ethanol, 15 mL of H_2O, and 4.5 mL of $NH_3{\cdot}H_2O$ (25 wt%), under continuous vigorous stirring for 20 min at 25°C. Afterward, 0.6 g resorcinol and 0.84 mL formaldehyde (37 wt%) were added to the above solution with stirring for 24 h at 25°C. The sediment was separated by centrifugation, washed with ethanol and water, and dried at 80°C for 12 h to obtain the SiO_2@SiO_2/RF (RF: resorcinol/formaldehyde) nanospheres. Subsequently, MCSs were obtained after carbonization at 800°C under N_2 for 5 h and removing silica templates by hydrofluoric acid. Finally, the NMCS was obtained by annealing the MCS sample at 800°C for 60 min under NH_3 gas flow.

Synthesis of AF hydrogel electrolyte (AF-gel)

First, 4 g acrylamide was dissolved in 20 mL deionized water with vigorous stirring for 0.5 h, followed by the addition of 2.5 mg *N*,*N*′-methylenebisacrylamide, 20 mg *N*,*N*,*N*′,*N*′-tetramethylethylenediamine, and 20 mg ammonium persulfate into the solution. The above solution was stirred until it became clear. Afterward, the obtained solution was injected into a plastic mold and stored at 60°C to polymerize. Subsequently, the as-prepared sample was soaked in a 30 volume% ethylene glycol (EG) solution of 1 mol L^{-1} $ZnSO_4$ for 24 h.

Assembly of ZHSCs

The coin-type cells comprised the NMCS electrode, commercial Zn foil, 1 mol L^{-1} $ZnSO_4$ aqueous solution, and glass fiber membrane as the cathode, anode, electrolyte, and separator, respectively. The NMCS cathode is composed of 80 wt% of NMCS, 10 wt% of acetylene black and 10 wt% of polytetrafluoroethylene. The above mixture was mixed in ethanol to form a uniform slurry, and the slurry was pressed onto stainless steel. The as-prepared electrodes were dried in a vacuum oven at 85°C overnight. The average loading of the active material was 1.0 to 1.2 mg cm^{-2}. The AF quasi-solid-state ZHSCs were constructed by sandwiching NMCS cathode, AF-gel separator, and Zn anode together. This device was encapsulated by polypropylene tape to further improve the service life.

Preparation of quasi-solid-state planar ZHSCs

First, an interdigital Ag electrode was prepared on a flexible polyethylene terephthalate (PET) substrate through screen printing. The NMCS was mixed with acetylene black and poly(vinylidene fluoride) binder at a weight ratio of 7:1:2 in 1-methyl-2-pyrrolidinone (NMP). Subsequently, the slurry was screen-printed on one side of the Ag interdigital electrode several times. The Zn nanosheets were electrochemically deposited on the other side of the Ag interdigital electrode by employing a three-electrode system. In detail, 0.5 g of boric acid, 3.2 g of zinc sulfate heptahydrate, and 3.2 g of Na_2SO_4 were dissolved in 50 mL deionized water and used as the electrolyte. A Pt foil and Ag/AgCl served as the counter electrode and the reference electrode, respectively. Electrodeposition was conducted with a constant current density of −20 mA cm^{-2} for 20 min. Then, the fabricated interdigital Zn electrode was washed with deionized water and dried at 60°C overnight in a vacuum oven. Next, a piece of hydrogel electrolyte was coated with copper tape on the patterned electrodes employed as the current collectors. Finally, the planar ZHSC was placed between two thermoplastic films and thermoplastically sealed.

RESULTS AND DISCUSSION

The preparation procedure of the NMCSs is schematically illustrated in Fig. 1a. With the use of tetrapropyl orthosilicate as a template agent, resorcinol-formaldehyde (RF) oligomers were synthesized onto the SiO_2 core nanoparticles, forming the SiO_2@SiO_2/RF precursor. After the carbonization and the removal of the template, the as-prepared MCSs were further treated by ammonia treatment to fabricate NMCSs. Morphology investigation by SEM and transmission electron microscopy (TEM) shows that SiO_2@SiO_2/C (Fig. 1b and Fig. S1) perfectly inherited the architecture of SiO_2@SiO_2/RF (Fig. S2) with an average size of ~250 nm. After the SiO_2 template was removed, the MCSs presented a hollow morphology with radial pore

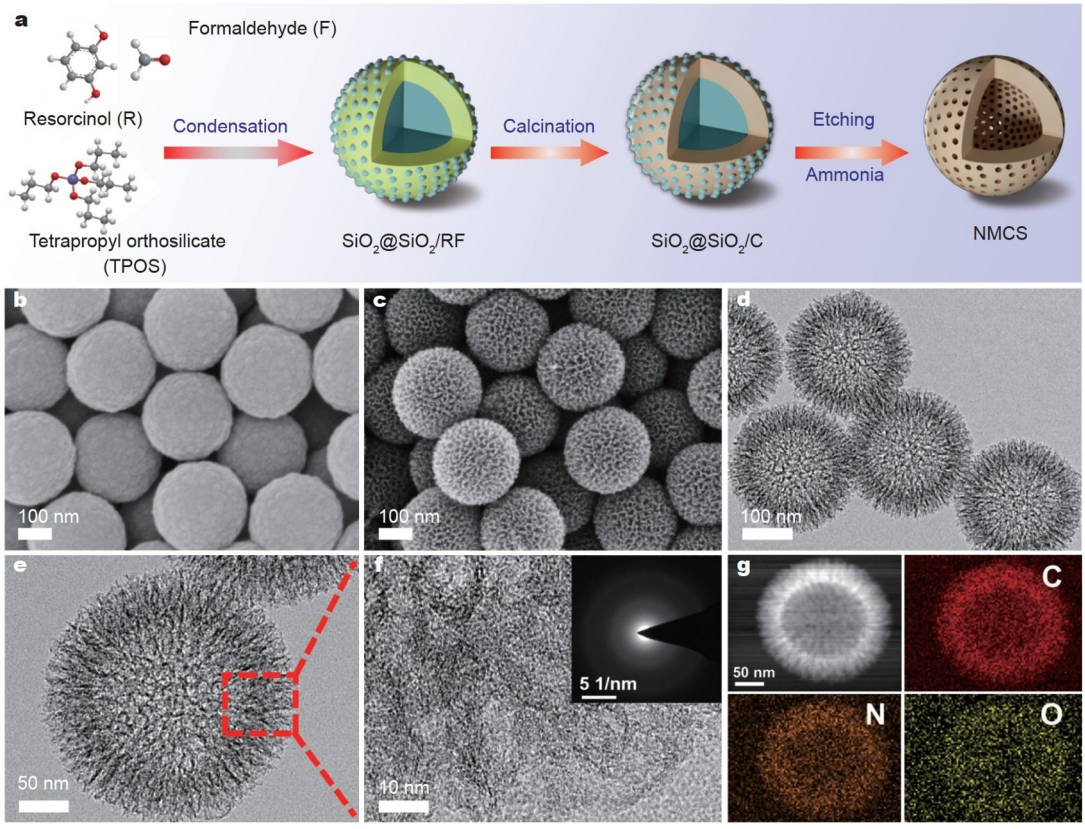

Figure 1 (a) Schematic illustration of the fabrication of NMCSs. SEM images of (b) SiO_2@SiO_2/C and (c) NMCSs. (d, e) TEM and (f) high-resolution TEM images of NMCSs. The inset is the corresponding selected area electron diffraction (SAED) pattern. (g) HAADF-STEM image and corresponding elemental mappings of NMCSs.

channels throughout the whole nanosphere (Fig. S3). The MCSs can transform into NMCSs with abundant graphene-like edges after subsequent ammonia treatment (Fig. 1c–f), which can help provide a high reaction activity for Zn^{2+} storage [20,21]. The C, N, and O elements that are distributed uniformly in NMCSs are shown by high-angle annular dark-field scanning TEM (HAADF-STEM) and corresponding elemental mapping (Fig. 1g). The corresponding XRD patterns present two broad diffraction peaks of (002) and (100) crystal planes that are characteristics of graphitic carbon (Fig. S4a), which is consistent with the TEM results [22,23]. The chemical composition of NMCSs was further investigated by XPS. The oxygen functional group is proven to be –OH at 285.3 eV in C 1s XPS spectra (Fig. S4b) and further verified by O 1s XPS spectra (Fig. S4c) [24]. In addition, three kinds of various nitrogen functional groups are graphitic N (401.4 eV), pyrrolic N (399.9 eV), and pyridinic N (398.2 eV) from N 1s XPS spectra (Fig. S4d) [13,25]. Nitrogen adsorption-desorption isotherms indicate that MCSs and NMCSs display characteristics of type IV isotherm with a typical hysteresis loop, which is assigned to the coexistence of mesoporous characteristics (Fig. S5). The Brunauer-Emmett-Teller surface areas of NMCSs and MCSs are 1511 and 1357 $m^2 g^{-1}$, respectively. In addition, the pore size distribution curve demonstrates that the NMCSs have a hierarchical porous characteristic, with three types of pore sizes situated at about 1.1, 4.2, and 7.5 nm (insets of Fig. S5). The high specific surface area and hierarchically microporous structure are favorable for promoting the adsorption/desorption process, thus improving the surface capacitive capacity and rate capability. Moreover, the NMCSs became more hydrophilic because of nitrogen doping, confirmed by the decreased water contact angles from 85.6° to 61.9° (Fig. S6). The superior surface wettability is prone to reduce the interfacial resistance between the electrode and the electrolyte, thereby further improving the kinetics of Zn^{2+} diffusion.

An aqueous ZHSC (denoted as NMCS ZHSC) was constructed by employing NMCSs as the cathode and Zn foil as the anode in 1 mol L^{-1} $ZnSO_4$ electrolyte to investigate the electrochemical performance of the NMCS electrode. The cyclic voltammetry (CV) curves in Fig. S7a reveal a wide potential difference between NMCS cathode and Zn anode. The strong redox peaks at −1.2/−0.85 V (*versus* SCE) observed on the Zn anode correspond to the plating/stripping process of Zn/Zn^{2+}. It is disclosed that CV curves in the initial five cycles changed slightly, and almost 100% of initial capacitance was kept (Fig. S7b), demonstrating excellent stability and reversibility of NMCS ZHSCs. The CV curves of the NMCS ZHSC are nearly similar to the enhanced scan rates from 5 to 300 mV s^{-1} between 0.2 and 1.8 V (Fig. 2a), thereby indicating rapid reaction kinetics and outstanding rate performance. The CV curves (Fig. S8a) of the MCS ZHSC also maintain a similar shape as the CV curves of NMCS ZHSCs, but the corresponding integral area is smaller at the same scan rates. The increased rate capability of the NMCS electrode can also be confirmed by the galvanostatic charge/discharge (GCD) test. The NMCS ZHSC can be steadily charged/discharged at current densities ranging from 0.2 to 50 A g^{-1} (Fig. 2b), which is better than that of MCS ZHSCs (Fig. S8b). Profiting from the nitrogen doping and hierarchical

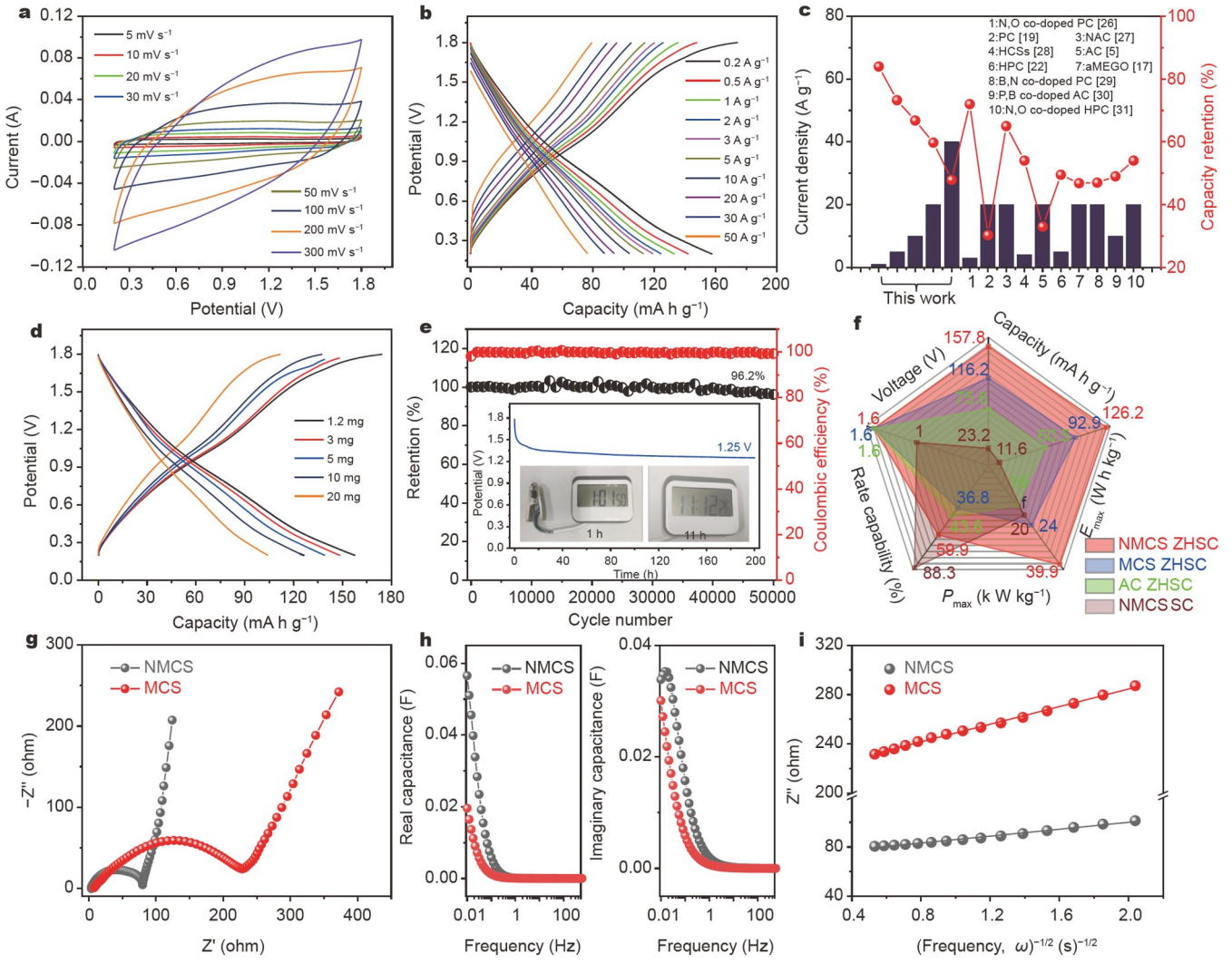

Figure 2 (a) CV curves of NMCS ZHSC at various scan rates. (b) GCD curves of NMCS ZHSC at various current densities. (c) Comparison of rate performance for NMCS ZHSC with state-of-the-art reported ZHSCs. (d) GCD curves of NMCS ZHSC with different mass loadings at 0.2 A g^{-1}. (e) Cycling stability and Coulombic efficiency of NMCS ZHSC at 5 A g^{-1}. The insets show the self-discharge curve during self-discharging for 200 h and the photographs of a smart timer operated by a ZHSC for 11 h. (f) The radar chart compares the five figures of merit of ZHSCs based on NMCS, MCS, AC, and NMCS SC: capacity, E_{max}, P_{max}, rate capability (from 0.2 to 20 A g^{-1}), and working voltage. (g) Nyquist plots, (h) real or imaginary part of capacitance against frequency, and (i) linear fitting to Z' against $\omega^{-1/2}$ plots in the low frequency range of NMCS and MCS electrodes.

mesopore structure, the NMCS-derived ZHSC delivers a good specific capacity of 157.8 mA h g^{-1} at 0.2 A g^{-1}, which is higher than those of ZHSCs based on MCSs (116.2 mA h g^{-1}) and AC (75.6 mA h g^{-1}) (Fig. S9a). The GCD curves at 0.5 A g^{-1} (Fig. S9b) show that the internal resistance (IR) voltage drops of the NMCS-, MCS-, and AC-based ZHSCs were 0.012, 0.023, and 0.026 V, respectively, thus proving that the NMCS electrode has the best electrolyte infiltration. Moreover, the NMCS ZHSC displays the best rate capability with a good capacity retention of 76.4 mA h g^{-1} at 50 A g^{-1}; these values were only 30.8 mA h g^{-1} at 30 A g^{-1} for MCS ZHSC and 33.0 mA h g^{-1} at 20 A g^{-1} for AC ZHSC. Clearly, the NMCS ZHSC demonstrates not only high specific capacity but also excellent rate capability, which outstrips those of the previously reported aqueous ZHSC (Fig. 2c) [5,17,19,22,26–31]. Moreover, the NMCS electrode displays remarkable capacity retention with increasing mass loadings of 1.2, 3, 5, 10, and 20 mg cm^{-2} because of fast ion transport ascribed to the hierarchical mesoporous structure. A large capacity of 104.2 mA h g^{-1} for NMCSs with a high 20 mg cm^{-2} loading is also maintained at 0.2 A g^{-1} (Fig. 2d), thereby further showing that the NMCS is a promising cathode for Zn^{2+} storage.

The NMCS ZHSC shows good cycling stability with a high capacity retention of 96.2% after 50,000 cycles at 5 A g^{-1} and approximately 100% Coulombic efficiency (Fig. 2e). The inset of Fig. 2e shows the self-discharge performance of the NMCS ZHSC device for 200 h. The NMCS ZHSC can still hold a high voltage of 1.35 V after 24 h self-discharge, lowering only to 1.25 V after 200 h, which outperforms the corresponding MCS ZHSC and NMCS symmetric SC (NMCS SC) (Fig. S10). This is because low and stable Zn anode potential of −0.76 V (*versus* SHE) is conducive to stabilizing the electric field inside ZHSCs, thereby inhibiting anion desorption from the cathode surface and self-discharge property of the ZHSCs. A single NMCS ZHSC can easily operate a smart timer for more than 11 h, thereby suggesting its superior self-discharge rate. Interestingly, the morphology of NMCSs was preserved well after 50,000 cycles at

5 A g^{-1} (Fig. S11a), and no obvious Zn dendrites were observed from the Zn foil (Fig. S11b), which coincide with the excellent cycling stability of NMCS ZHSCs [32]. In addition, the NMCS ZHSCs with high mass loadings of 5 and 10 mg cm^{-2} at 5 A g^{-1} show high capacity retentions of 94.4% and 91.1% after 50,000 cycles, respectively (Fig. S12), indicating the excellent cycling stability of NMCS ZHSCs under high load conditions.

To highlight the advantages of NMCS ZHSCs, the electrochemical performance of the NMCS electrodes was investigated in symmetrical SCs with 1 mol L^{-1} H_2SO_4 electrolyte (Fig. S13). A radar chart (Fig. 2f) summarizes the five figures of merit of the highest capacities, maximal energy and power densities, rate capabilities, and working voltages for NMCS ZHSC, MCS ZHSC, AC ZHSC, and NMCS SC devices. The NMCS ZHSC has the largest capacity of 157.8 mA h g^{-1}, energy density of 126.2 W h kg^{-1}, and power density of 39.9 kW kg^{-1} among these devices, which are much higher than the previously reported results (Table S1). We also calculated the energy density of NMCS ZHSCs on the basis of the total mass of both Zn anode and NMCS cathode. The NMCS ZHSC still delivers a high energy density of 75.7 W h kg^{-1}. Remarkably, the aqueous NMCS ZHSC possesses higher capacity, energy density, and power density than aqueous NMCS SC. However, the NMCS SC demonstrates superior rate capability because of the quick adsorption/desorption mechanism of EDLC [13]. Electrochemical impedance spectroscopy (EIS) tests were conducted to verify the charge transfer and Zn^{2+} diffusion kinetics of NMCSs (Fig. 2g). The charge transfer resistance (R_{ct}) and Warburg impedance (Z_w) of NMCSs are smaller than those of MCSs, indicating that the NMCS is more effective for fast charge transfer and ion diffusion at the electrode/electrolyte interface [33]. The complex model of the capacitance was employed to estimate the capacitance variations, with the real capacitance ($C'[\omega]$) and imaginary capacitance ($C''[\omega]$) extracted from the EIS data (Fig. 2h) [34]. The time constant (τ_0), defined as $\tau_0 = 1/f$ (f corresponds to the characteristic frequency of a phase angle at 45°), expresses the time duration that is required to deliver the stored energy and power effectively [35]. The NMCSs possess a higher capacitance in the low frequency region and quicker Zn^{2+} diffusion, as demonstrated by the distinctly reduced τ_0 value of NMCSs (~68 s) compared with that of MCSs (~100 s). The faster Zn^{2+} diffusion in NMCSs is also confirmed by the lower Warburg coefficient (σ) (Fig. 2i). The diffusion coefficient (D) of Zn^{2+} under the interfacial region is calculated as 2.77×10^{-11} and 1.81×10^{-10} cm^2 s^{-1} for MCSs and NMCSs, respectively.

The surface capacitive contribution and diffusion-controlled process were investigated from the CV curves of NMCS and MCS ZHSCs to further understand the electrochemical dynamic behavior and reaction kinetics. As shown in Fig. 3a and Fig. S14, capacitive charge contributions play a dominant role in NMCS ZHSCs (76.1%) and MCS ZHSCs (63.2%) at 30 mV s^{-1}. Moreover, the surface capacitive contribution in NMCS ZHSCs is 63.5% at 5 mV s^{-1}, reaching 96.4% at 100 mV s^{-1} (Fig. 3b), thus indicating effective surface charge storage and excellent reversibility. The calculated b values of the NMCS ZHSC are 0.922 and 0.909 for the anodic and cathodic peak currents, respectively (Fig. 3c), thereby indicating that the charge storage process is dominated by the surface charge storage behavior, which is beneficial to accelerating Zn^{2+} diffusion [36]. The results show that the hierarchical mesoporous structure of NMCSs possesses abundant Zn^{2+} active sites and fast diffusion channels, leading to superior rate performance. A series of *ex-situ* tests were conducted during the second triangular GCD curve of the NMCS ZHSC and the selected charging/discharging states to better investigate the energy storage mechanism of NMCS ZHSCs (Fig. 3d). The surface of Zn foil develops a rough morphology with nanosheets during the discharge-charge process (Fig. S15). The *ex-situ* XRD patterns of Zn foil (Fig. S16) suggest that the diffraction intensities of (002) gradually reduce as the (101) peak increases during the discharging states (A→C); this phenomenon was reversed during the charging process (C→E), indicating the crystalline structural evolution of Zn anode during the exfoliating and depositing conversion [31]. For the NMCS cathode, the flaky $Zn_4SO_4(OH)_6{\cdot}5H_2O$ nanosheets gradually increase during the discharge process, whereas they exhibit a fully converse variation process during the charging process (Fig. S17). The reversible formation/dissolution procedures of $Zn_4SO_4(OH)_6{\cdot}5H_2O$ are also proven from the corresponding *ex-situ* XRD patterns variation during the discharge-charge states (Fig. S18), thereby revealing that the electrochemically active sites on the NMCS were hardly damaged [5,37]. The *ex-situ* C 1s XPS spectra are examined to analyze the chemical structure variation in detail (Fig. 3e). The two peaks at 284.4 and 285.3 eV are attributed to C–C and C–OH functional groups, respectively. The peak intensities of C–OH gradually reduce during the discharge process and then increase during the charging process, indicating that C–OH participates in reversible Faradaic charge storage with good reversibility [19]. Moreover, the peak at 286.4 eV corresponding to C–O–Zn bonding is detected at 0.2 V and gradually reduce during the charging process, implying that the faradaic reactions did happen by the chemical interaction between hydroxyl groups and Zn ions. For O 1s XPS spectra (Fig. 3f), the peak intensities of the carbonyl (C=O) decrease continuously during the charge courses and then increase gradually during the discharge process, indicating that the transformations of partial C=O groups are highly reversible during the charge/discharge processes [20,38]. The C=O groups can be reversibly converted to hydroxyl groups by gaining and losing electrons during charge/discharge processes. Furthermore, the contents of C, N, O, Zn, and S elements are explored by X-ray electron diffraction spectroscopy (EDS) at different charging/discharging states. As shown in Fig. S19, the contents of Zn and S increase from states A to C and decrease to state E. The EDS mapping results suggest that C, O, N, and Zn elements are distributed homogeneously (Fig. S20), thereby further proving that $Zn_4SO_4(OH)_6{\cdot}5H_2O$ can be likely formed during the charge processes and partially resolved during the discharge processes [39–42].

To acquire a deeper understanding of the energy storage mechanism of ZHSCs, *in-situ* EQCM measurement was conducted to examine the mass change of active materials during real-time charge and discharge processes (Fig. 3g) [43,44]. Fig. S21a shows the raw CV curves of the NMCS electrode, which exhibits a perfectly capacitive CV response characteristic. As shown in Fig. S21b, c, the variations of potential, resonance frequency, and charge are almost the same from the first to the fourth electrochemical cycles. Therefore, the mass change of NMCSs in an electrochemical cycle from the raw data can be calculated by using the Sauerbrey equation [45]. During the discharge process, the electrode mass change is not obvious from 1.8 to 1.0 V, which can be related to the balance of the Zn^{2+} adsorption and SO_4^{2-} desorption at the carbon surface (Fig. 3h).

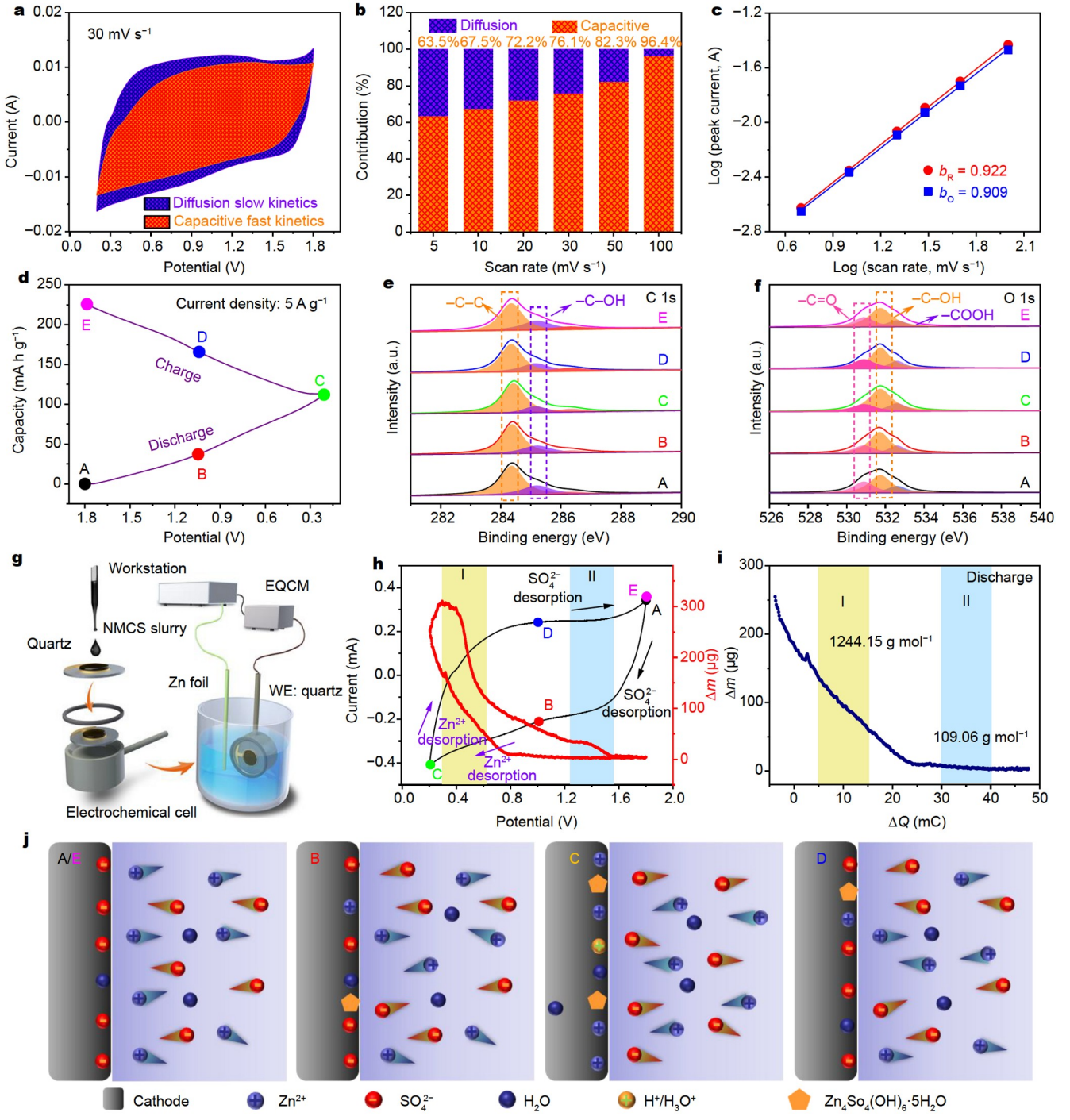

Figure 3 (a) CV curves with a capacitive contribution at 30 mV s^{-1}, (b) capacitive contributions at various scan rates, and (c) the fitting plot between log(*i*) and log(*v*) of NMCS ZHSCs. (d) Discharge/charge curve at 5 A g^{-1} of NMCS ZHSCs. The corresponding *ex-situ* XPS spectra of (e) C 1s and (f) O 1s. (g) Schematic of an *in-situ* EQCM setup. (h) CV curves and the corresponding mass change during the charge and discharge processes, and (i) mass *versus* charge curve during the discharge process. (j) Schematic of the adsorption/desorption of ions for the NMCS electrode during the charge and discharge processes.

The electrode mass change is significantly increased during 1.0 to 0.2 V, which can be attributed to the successive anion desorption process. In addition, the *ex-situ* XRD and SEM results show that the progressive increase in the mass is associated with the formation of $Zn_4SO_4(OH)_6·5H_2O$. In contrast, the electrode mass shows a conspicuous decrease during the charging process from 0.2 to 1.8 V, which mainly involves the desorption of Zn^{2+} and the dissolution of $Zn_4SO_4(OH)_6·5H_2O$. As shown in Fig. 3i, the electrode mass change of the electrode *versus* the charge during the discharge process and the shaded areas represent the different ion adsorption or desorption processes. The average molecular weights (*M*/*z*) of the adsorbed ions calculated from the experimental slope are 1244.15 and 109.06 g mol^{-1} in region I at low potentials and region II at high potentials, respectively.

The M/z = 1244.15 g mol^{-1} is nearly equal to the species that includes two $Zn_4SO_4(OH)_6{\cdot}5H_2O$ (549.64 g mol^{-1}) and two Zn^{2+} (65.41 g mol^{-1}), and the M/z = 109.06 g mol^{-1} can be attributed to the species that includes three-Zn^{2+} (65.41g mol^{-1}) adsorption and one-SO_4^{2-} (96.06 g mol^{-1}) desorption. In addition, the M/z = 1223.84 g mol^{-1} can be assigned to the species that includes two $Zn_4SO_4(OH)_6{\cdot}5H_2O$ and two Zn^{2+} during the charging process (Fig. S21d), supporting the dissolution of $Zn_4SO_4(OH)_6{\cdot}5H_2O$ and desorption of Zn^{2+} during the charging process. Moreover, the H^+ or H_3O^+ adsorption of the NMCS electrode would enhance the pH value of the electrolyte, which leads to increased mass by the precipitation of $Zn_4SO_4(OH)_6{\cdot}5H_2O$ [11]. Also, the mass decrease during the charging process is attributed to the dissolution of $Zn_4SO_4(OH)_6{\cdot}5H_2O$ in the high potential region. Thus, the reversible adsorption of Zn^{2+} and SO_4^{2-} occurred in different potential ranges (Fig. 3j). Typically, the Zn^{2+} adsorption/desorption on the cathode surface mainly occurred at low voltages, and SO_4^{2-} adsorption/desorption principally took place at high voltages. Moreover, the adsorption/desorption of SO_4^{2-} and Zn^{2+} simultaneously occurred in the medium-potential region. Meanwhile, the invertible chemical adsorption of oxygen functional groups also occurred during the charge/discharge processes, providing good capacitive performance. Also, the $Zn_4SO_4(OH)_6{\cdot}5H_2O$ reversible formation/dissolution can occur during the charge/discharge processes at low voltages.

To demonstrate the flexible application of the ZHSCs, we assembled a quasi-solid-state device by using AF polyacrylamide (PAM) hydrogel as the electrolyte (Fig. 4a). The as-prepared PAM was completely soaked with a mixed solution of EG, H_2O, and $ZnSO_4$ to obtain the AF-gel during the exchange of water in the hydrogel network with EG (Fig. 4b). In the AF-gel, EG forms stable molecular clusters to compete with hydrogen bonds in water, which results in the decreased saturated vapor pressure of water [46,47]. The mass retention of all components in AF-gel is evaluated and presented in Fig. S22. SEM images of the freeze-dried AF-gel show a large number of micropores (Fig. S23), which facilitate fast ion diffusion. The ionic conductivities of AF-gel electrolyte under 25, 0, and −20°C are 15.65, 12.63, and 8.84 mS cm^{-1}, respectively, as confirmed by the electrochemical

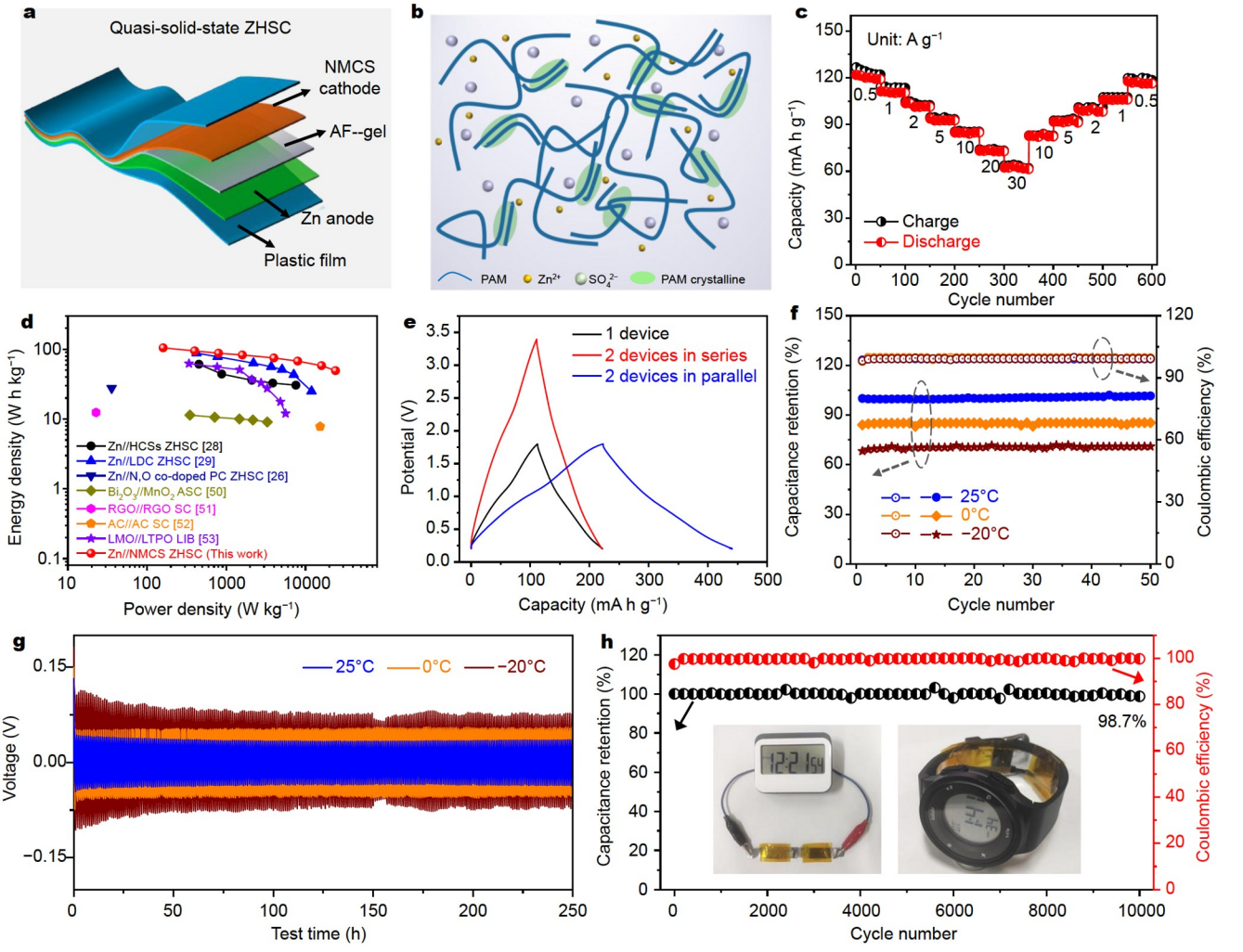

Figure 4 (a) Structural diagram of the quasi-solid-state NMCS ZHSC device. (b) Schematic of the structure of AF-gel. (c) Rate performance of the NMCS ZHSC. (d) Ragone plots for the quasi-solid-state NMCS ZHSC. (e) GCD curves of single, two-in-series/parallel devices at 5 A g^{-1}. (f) Cycling performances of the quasi-solid-state NMCS ZHSC at 25, 0, and −20°C. (g) Cycling performances of the Zn//Zn symmetrical cell with 0.5 mA cm^{-2} at 25, 0, and −20°C. (h) Cycling life and Coulombic efficiency of quasi-solid-state NMCS ZHSC (25°C) at 5 A g^{-1}. The insets show a smart timer or watch operated by two serially connected devices.

impedance test (Fig. S24) [48,49]. The CV and GCD curves (Fig. S25) exhibit that the energy storage capacity of the quasi-solid-state ZHSC is highly comparable to the values in aqueous electrolytes. Its highest capacity reaches 130.9 mA h g^{-1} at 0.2 A g^{-1}, and 61.6 mA h g^{-1} is still retained even at a high current density of 30 A g^{-1} (Fig. 4c). Specifically, its energy density of 104.7 W h kg^{-1} considerably overmatches the majority of recently reported quasi-solid-state SCs [26,28,29,50–52] and LIBs [53] (Fig. 4d). To boost the operating voltage, two devices connected in series can offer a wide voltage of 3.4 V, and the capacity is doubled in parallel (Fig. 4e). This NMCS ZHSC can retain 85.4% (at 0°C) and 71.1% (at −20°C) of specific capacity (at 25°C) at 1 A g^{-1} together with a high Coulombic efficiency of ~100%, indicating its good AF property and high ionic conductivity at low temperatures (Fig. 4f). In addition, we investigated the long-term cycling properties of Zn plating/stripping in the Zn//Zn symmetrical cells with AF-gel electrolyte at different temperatures. As shown in Fig. 4g, the symmetric Zn cell exhibits a stable polarization voltage and cycle performance exceeding 250 h at 0.5 mA cm^{-2} under 25, 0, and −20°C. More interestingly, the cycling stability of the assembled NMCS ZHSC was investigated at 5 A g^{-1}, displaying impressive values of 98.7%, 94.1%, and 86.3% of their original capacity retention at 25, 0, and −20°C, respectively, and near 100% Coulombic efficiency after 10,000 charge/discharge cycles (Fig. 4h and Fig. S26). A smart timer or watch can be operated easily using two devices in series (as seen from the insets of Fig. 4h). These results further confirm that the designed ZHSC possesses promising flexible application in a wide temperature range.

We further demonstrated a new type of planar ZHSCs *via* facile screen printing and electrochemical deposition techniques for use in miniaturized and wearable electronic applications (Fig. 5a). First, the Ag interdigital electrode is deposited, followed by screen printing the NMCS cathode and electrodepositing the Zn nanosheet anode. The SEM images show that the vertical Zn nanosheets are uniformly grown on the surface of Ag interdigital fingers (Fig. S27), which will accelerate the charge transport and hinder the growth of Zn dendrites. The XRD pattern (JCPDS No. 04-0831) and XPS spectrum confirm the composition of Zn nanosheets (Fig. S28) [54,55]. The CV curves (Fig. 5b) at various scan rates present a nearly rectangular shape, thereby illustrating the excellent rate capability of the planar

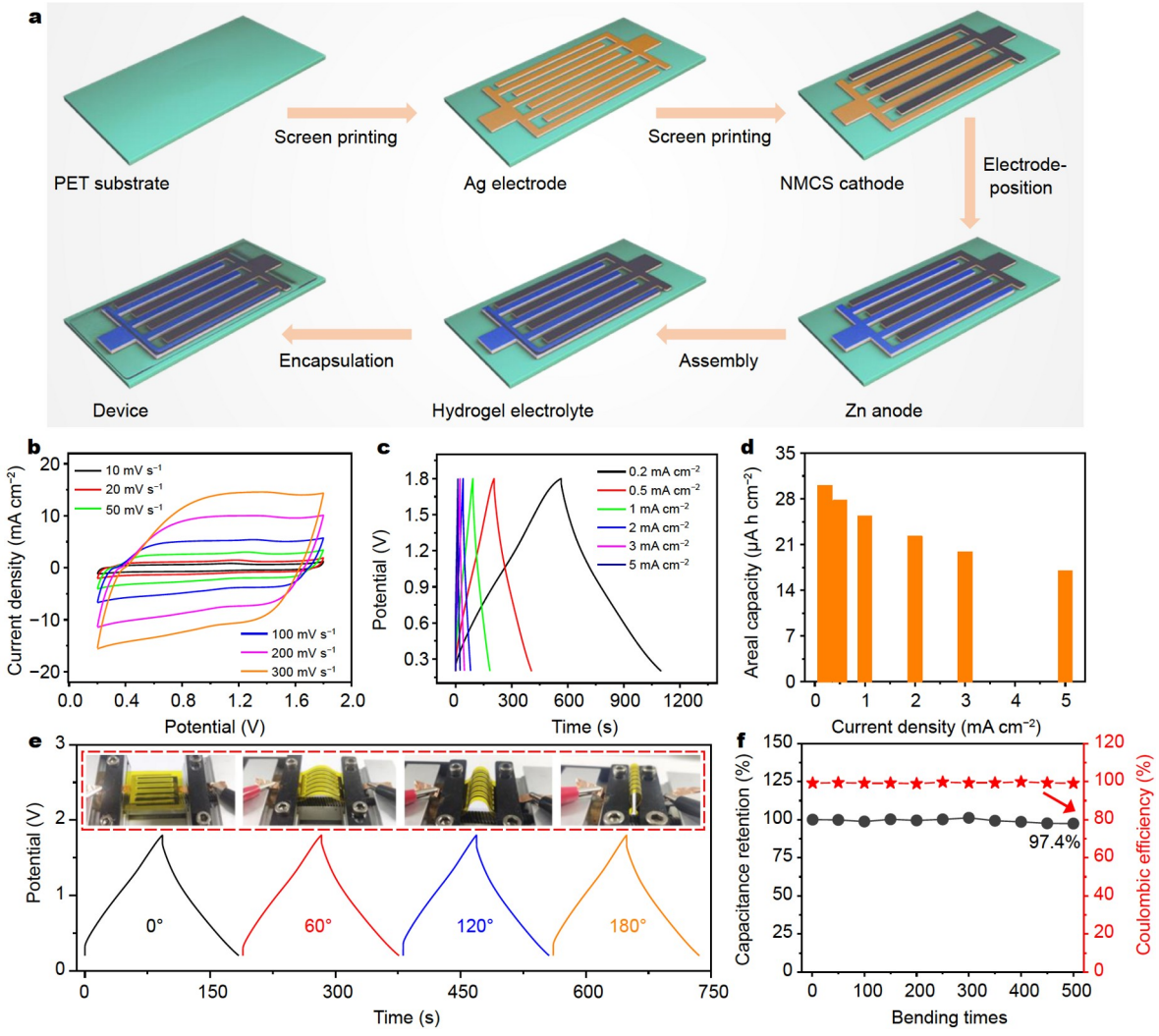

Figure 5 (a) Fabrication process for the quasi-solid-state planar ZHSC. (b) CV curves of the planar ZHSC at various scan rates. (c) GCD curves at various current densities. (d) Areal capacity and rate capability. (e) GCD curves at 1 mA cm^{-2} of the planar ZHSC under different bending angles from 0° to 180°. (f) Capacitance retention against bending times at 1.0 mA cm^{-2}.

ZHSCs. The GCD curves (Fig. 5c) show symmetrical and linear shapes with no obvious internal resistance drop. The highest areal capacity of the device reaches 30.0 μA h cm^{-2} at 0.2 mA cm^{-2} and 16.9 μA h cm^{-2} even at 5.0 mA cm^{-2} (Fig. 5d). To estimate the exceptional mechanical flexibility of the planar ZHSC, the device was subjected to mechanical bending from 0° to 180°. Remarkably, the GCD curves remained almost the same when bent from a flat position to a 180° angle (Fig. 5e), demonstrating remarkable flexibility. Surprisingly, the planar ZHSC retained 97.4% of the initial capacity and ~100% of the Coulombic efficiency after being bent 500 times (Fig. 5f).

The electrochemical performance of the planar ZHSC was also investigated at 25, 0, and −20°C. The planar ZHSC can retain 90.3% (at 0°C) and 80.1% (at −20°C) of its specific capacity (at 25°C) at 0.2 mA cm^{-2} (Fig. 6a), which is attributed to the good AF property of the AF-gel. More significantly, the cycling stability of planar ZHSC was tested at 1 mA cm^{-2}, displaying excellent capacitance retention of 97.6%, 94.8%, and 88.4 % at 25, 0, and −20°C after 5000 charge/discharge cycles (Fig. 6b), respectively, demonstrating that the planar ZHSC can provide stable power output in low-temperature environments. The Zn anode still retains its nanosheet morphology, and no Zn dendrite was formed after cycling measurement at 25°C (Fig. S29), thereby proving that the Zn nanosheets have excellent reversibility and stability [16]. In addition, we investigated the self-discharge performance of the planar ZHSC (Fig. S30). The operating voltage was retained at 1.2 V after 24 h self-discharge, indicating that the planar ZHSC has remarkable thermodynamic stability. The operating voltage or output current of the device can be readily expanded by continuous integration of electrode arrays in series. The CV curves (Fig. 6c) of the device from 1 to 3 planar ZHSCs in series display similar capacitive shapes at 50 mV s^{-1} and show a linear increase at an operating voltage ranging from 1.6 to 5.0 V, which is well supported by GCD curves (Fig. 6d), thereby indicating outstanding performance uniformity [56,57]. The Ragone plots shown in Fig. 6e compare the planar ZHSCs in this work with other commercially available energy storage devices. The planar ZHSC offers an ultra-high volumetric energy density of 31.6 mW h cm^{-3}, which is much higher than those of most reported planar SCs (Table S2) and commercially available energy storage devices [58,59]. Finally, we demonstrate that a smart timer can be easily operated under different destruction conditions by a planar ZHSC (Fig. 6f). We believe that this work not only offers enlightening insights for designing high-performance ZHSCs but also shows a potential perspective for integration in flexible electronic devices.

CONCLUSIONS

In summary, a ZHSC with excellent capacitive performance is demonstrated by coupling highly reversible NMCSs as the cathode in an aqueous electrolyte. The hierarchically mesoporous architecture and nitrogen doping endow NMCSs with fast ion/electron transport and a highly accessible surface area to achieve efficient Zn^{2+} storage. The as-assembled aqueous NMCS ZHSC displays a remarkable capacity of 157.8 mA h g^{-1}, an extremely high energy density of 126.2 W h kg^{-1}, a superb power density of 39.9 kW kg^{-1} with an ultra-fast charge time of 5.5 s, and outstanding cycling stability (96.2% capacity retention after 50,000 cycles), which is substantially superior to those of most previously reported ZHSCs. Moreover, a new type of planar ZHSC is demonstrated with outstanding low-temperature electrochemical performance, ultra-high volumetric energy density, and outstanding serial and parallel modularization for improving the voltage and current output. *Ex-situ* XRD, XPS, SEM, and

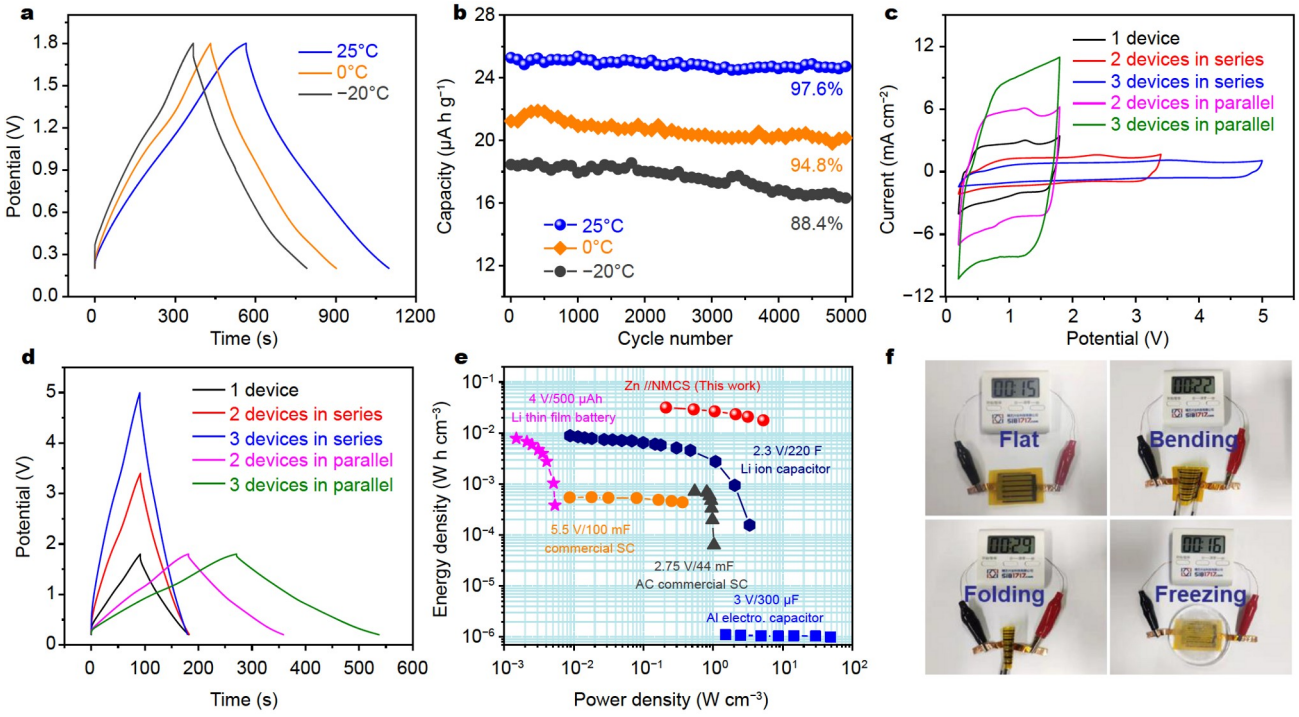

Figure 6 (a) GCD curves at 0.2 mA cm^{-2} and (b) cycling performances at 1 mA cm^{-2} of the planar ZHSC at 25, 0, and −20°C. (c) CV curves and (d) GCD curves of single, series, and parallel connections of planar ZHSC. (e) Ragone plots comparing the energy and power density of planar ZHSC with those of commercially available energy storage devices. (f) Photographs of the planar ZHSC powering a smart timer under different conditions.

in-situ EQCM experiments verify that the superior electrochemical capability is due to the synergistic effect of cation and anion adsorption, as well as the reversible chemical adsorption of NMCSs during charge/discharge processes. Thereby, this work provides not only enlightening insights for designing cathode materials and novel Zn^{2+} storage devices with high energy density and electrochemical stability, but also a deeper understanding of the electrochemical characteristics of ZHSCs.

Received 25 December 2021; accepted 21 February 2022; published online 12 April 2022

1 Simon P, Gogotsi Y. Perspectives for electrochemical capacitors and related devices. Nat Mater, 2020, 19: 1151–1163
2 Wang F, Wu X, Yuan X, *et al.* Latest advances in supercapacitors: From new electrode materials to novel device designs. Chem Soc Rev, 2017, 46: 6816–6854
3 Guo W, Yu C, Li S, *et al.* Toward commercial-level mass-loading electrodes for supercapacitors: Opportunities, challenges and perspectives. Energy Environ Sci, 2021, 14: 576–601
4 El-Kady MF, Strong V, Dubin S, *et al.* Laser scribing of high-performance and flexible graphene-based electrochemical capacitors. Science, 2012, 335: 1326–1330
5 Dong L, Ma X, Li Y, *et al.* Extremely safe, high-rate and ultralong-life zinc-ion hybrid supercapacitors. Energy Storage Mater, 2018, 13: 96–102
6 Ma H, Chen H, Wu M, *et al.* Maximization of spatial charge density: An approach to ultrahigh energy density of capacitive charge storage. Angew Chem Int Ed, 2020, 59: 14541–14549
7 Ma L, Zhao Y, Ji X, *et al.* A usage scenario independent "air chargeable" flexible zinc ion energy storage device. Adv Energy Mater, 2019, 9: 1900509
8 Peng Z, Huang J, He Q, *et al.* Green quasi-solid-state planar asymmetric supercapacitors with high working voltage and extraordinary volumetric energy density. J Mater Chem A, 2021, 9: 14363–14371
9 Wu Y, Tao Y, Zhang X, *et al.* Self-assembled α-MnO_2 urchin-like microspheres as a high-performance cathode for aqueous Zn-ion batteries. Sci China Mater, 2020, 63: 1196–1204
10 An GH, Hong J, Pak S, *et al.* 2D metal Zn nanostructure electrodes for high-performance Zn ion supercapacitors. Adv Energy Mater, 2019, 10: 1902981
11 Dong L, Yang W, Yang W, *et al.* High-power and ultralong-life aqueous zinc-ion hybrid capacitors based on pseudocapacitive charge storage. Nano-Micro Lett, 2019, 11: 94–102
12 Zheng Y, Zhao W, Jia D, *et al.* Porous carbon prepared *via* combustion and acid treatment as flexible zinc-ion capacitor electrode material. Chem Eng J, 2020, 387: 124161
13 Yuksel R, Buyukcakir O, Panda PK, *et al.* Necklace-like nitrogen-doped tubular carbon 3D frameworks for electrochemical energy storage. Adv Funct Mater, 2020, 30: 1909725
14 Tang H, Yao J, Zhu Y. Recent developments and future prospects for zinc-ion hybrid capacitors: A review. Adv Energy Mater, 2021, 11: 2003994
15 Li Z, An Y, Dong S, *et al.* Progress on zinc ion hybrid supercapacitors: Insights and challenges. Energy Storage Mater, 2020, 31: 252–266
16 Zhang P, Li Y, Wang G, *et al.* Zn-ion hybrid micro-supercapacitors with ultrahigh areal energy density and long-term durability. Adv Mater, 2019, 31: 1806005
17 Wu S, Chen Y, Jiao T, *et al.* An aqueous Zn-ion hybrid supercapacitor with high energy density and ultrastability up to 80 000 cycles. Adv Energy Mater, 2019, 9: 1902915
18 Wang H, Wang M, Tang Y. A novel zinc-ion hybrid supercapacitor for long-life and low-cost energy storage applications. Energy Storage Mater, 2018, 13: 1–7
19 Yin J, Zhang W, Wang W, *et al.* Electrochemical zinc ion capacitors enhanced by redox reactions of porous carbon cathodes. Adv Energy Mater, 2020, 10: 2001705
20 Zhang H, Liu Q, Fang Y, *et al.* Boosting Zn-ion energy storage capability of hierarchically porous carbon by promoting chemical adsorption. Adv Mater, 2019, 31: 1904948
21 Fei R, Wang H, Wang Q, *et al. In situ* hard-template synthesis of hollow bowl-like carbon: A potential versatile platform for sodium and zinc ion capacitors. Adv Energy Mater, 2020, 10: 2002741
22 Yu P, Zeng Y, Zeng Y, *et al.* Achieving high-energy-density and ultrastable zinc-ion hybrid supercapacitors by engineering hierarchical porous carbon architecture. Electrochim Acta, 2019, 327: 134999
23 Jiang J, Yuan J, Nie P, *et al.* Hierarchical N-doped hollow carbon microspheres as advanced materials for high-performance lithium-ion capacitors. J Mater Chem A, 2020, 8: 3956–3966
24 Horikawa T, Sakao N, Sekida T, *et al.* Preparation of nitrogen-doped porous carbon by ammonia gas treatment and the effects of N-doping on water adsorption. Carbon, 2012, 50: 1833–1842
25 Hu X, Zhong G, Li J, *et al.* Hierarchical porous carbon nanofibers for compatible anode and cathode of potassium-ion hybrid capacitor. Energy Environ Sci, 2020, 13: 2431–2440
26 Lou G, Pei G, Wu Y, *et al.* Combustion conversion of wood to N, O co-doped 2D carbon nanosheets for zinc-ion hybrid supercapacitors. Chem Eng J, 2021, 413: 127502
27 Chang N, Li T, Li R, *et al.* An aqueous hybrid electrolyte for low-temperature zinc-based energy storage devices. Energy Environ Sci, 2020, 13: 3527–3535
28 Chen S, Ma L, Zhang K, *et al.* A flexible solid-state zinc ion hybrid supercapacitor based on co-polymer derived hollow carbon spheres. J Mater Chem A, 2019, 7: 7784–7790
29 Lu Y, Li Z, Bai Z, *et al.* High energy-power Zn-ion hybrid supercapacitors enabled by layered B/N co-doped carbon cathode. Nano Energy, 2019, 66: 104132
30 Lee YG, An GH. Synergistic effects of phosphorus and boron co-incorporated activated carbon for ultrafast zinc-ion hybrid supercapacitors. ACS Appl Mater Interfaces, 2020, 12: 41342–41349
31 Deng X, Li J, Shan Z, *et al.* A N, O co-doped hierarchical carbon cathode for high-performance Zn-ion hybrid supercapacitors with enhanced pseudocapacitance. J Mater Chem A, 2020, 8: 11617–11625
32 He H, Lian J, Chen C, *et al.* Super hydrophilic carbon fiber film for freestanding and flexible cathodes of zinc-ion hybrid supercapacitors. Chem Eng J, 2021, 421: 129786
33 Portet C, Yushin G, Gogotsi Y. Electrochemical performance of carbon onions, nanodiamonds, carbon black and multiwalled nanotubes in electrical double layer capacitors. Carbon, 2007, 45: 2511–2518
34 Nian YR, Teng H. Influence of surface oxides on the impedance behavior of carbon-based electrochemical capacitors. J Electroanal Chem, 2003, 540: 119–127
35 Shao Y, Sun Z, Tian Z, *et al.* Regulating oxygen substituents with optimized redox activity in chemically reduced graphene oxide for aqueous Zn-ion hybrid capacitor. Adv Funct Mater, 2020, 31: 2007843
36 Guo Q, Han Y, Chen N, *et al.* Few-layer siloxene as an electrode for superior high-rate zinc ion hybrid capacitors. ACS Energy Lett, 2021, 6: 1786–1794
37 Wan F, Zhang L, Dai X, *et al.* Aqueous rechargeable zinc/sodium vanadate batteries with enhanced performance from simultaneous insertion of dual carriers. Nat Commun, 2018, 9: 1656–1666
38 Huang Z, Wang T, Song H, *et al.* Effects of anion carriers on capacitance and self-discharge behaviors of zinc ion capacitors. Angew Chem Int Ed, 2021, 60: 1011–1021
39 Kundu D, Adams BD, Duffort V, *et al.* A high-capacity and long-life aqueous rechargeable zinc battery using a metal oxide intercalation cathode. Nat Energy, 2016, 1: 16119–16126
40 Ma X, Cheng J, Dong L, *et al.* Multivalent ion storage towards high-performance aqueous zinc-ion hybrid supercapacitors. Energy Storage Mater, 2019, 20: 335–342
41 Han D, Wu S, Zhang S, *et al.* A corrosion-resistant and dendrite-free zinc metal anode in aqueous systems. Small, 2020, 16: 2001736
42 Han D, Cui C, Zhang K, *et al.* A non-flammable hydrous organic electrolyte for sustainable zinc batteries. Nat Sustain, 2021, doi: 10.1038/s41893-021-00800-9
43 Salanne M, Rotenberg B, Naoi K, *et al.* Efficient storage mechanisms for building better supercapacitors. Nat Energy, 2016, 1: 16070–16079

44 Tsai WY, Taberna PL, Simon P. Electrochemical quartz crystal microbalance (EQCM) study of ion dynamics in nanoporous carbons. J Am Chem Soc, 2014, 136: 8722–8728
45 Zhang Q, Levi MD, Dou Q, *et al.* The charge storage mechanisms of 2D cation-intercalated manganese oxide in different electrolytes. Adv Energy Mater, 2019, 9: 1802707
46 Mo F, Liang G, Meng Q, *et al.* A flexible rechargeable aqueous zinc manganese-dioxide battery working at −20°C. Energy Environ Sci, 2019, 12: 706–715
47 Li Z, Chen D, An Y, *et al.* Flexible and anti-freezing quasi-solid-state zinc ion hybrid supercapacitors based on pencil shavings derived porous carbon. Energy Storage Mater, 2020, 28: 307–314
48 Zeng J, Dong L, Sun L, *et al.* Printable zinc-ion hybrid micro-capacitors for flexible self-powered integrated units. Nano-Micro Lett, 2020, 13: 19–32
49 Huang Y, Zhong M, Shi F, *et al.* An intrinsically stretchable and compressible supercapacitor containing a polyacrylamide hydrogel electrolyte. Angew Chem Int Ed, 2017, 56: 9141–9145
50 Xu H, Hu X, Yang H, *et al.* Flexible asymmetric micro-supercapacitors based on Bi_2O_3 and MnO_2 nanoflowers: Larger areal mass promises higher energy density. Adv Energy Mater, 2015, 5: 1401882
51 Zhang J, Jiang J, Li H, *et al.* A high-performance asymmetric supercapacitor fabricated with graphene-based electrodes. Energy Environ Sci, 2011, 4: 4009–4015
52 Yu H, Wu J, Fan L, *et al.* Improvement of the performance for quasi-solid-state supercapacitor by using PVA-KOH-KI polymer gel electrolyte. Electrochim Acta, 2011, 56: 6881–6886
53 Dong X, Chen L, Su X, *et al.* Flexible aqueous lithium-ion battery with high safety and large volumetric energy density. Angew Chem Int Ed, 2016, 55: 7474–7477
54 Sun G, Yang H, Zhang G, *et al.* A capacity recoverable zinc-ion micro-supercapacitor. Energy Environ Sci, 2018, 11: 3367–3374
55 Hao Z, Xu L, Liu Q, *et al.* On-chip Ni-Zn microbattery based on hierarchical ordered porous Ni@$Ni(OH)_2$ microelectrode with ultrafast ion and electron transport kinetics. Adv Funct Mater, 2019, 29: 1808470
56 Zhou F, Huang H, Xiao C, *et al.* Electrochemically scalable production of fluorine-modified graphene for flexible and high-energy ionogel-based microsupercapacitors. J Am Chem Soc, 2018, 140: 8198–8205
57 Zheng S, Tang X, Wu ZS, *et al.* Arbitrary-shaped graphene-based planar sandwich supercapacitors on one substrate with enhanced flexibility and integration. ACS Nano, 2017, 11: 2171–2179
58 El-Kady MF, Ihns M, Li M, *et al.* Engineering three-dimensional hybrid supercapacitors and microsupercapacitors for high-performance integrated energy storage. Proc Natl Acad Sci USA, 2015, 112: 4233–4238
59 Zheng S, Ma J, Wu ZS, *et al.* All-solid-state flexible planar lithium ion micro-capacitors. Energy Environ Sci, 2018, 11: 2001–2009

Acknowledgements This work was financially supported by the National Natural Science Foundation of China (52063019, 51973088, and 51761135114), the "Double Thousand Plan" Science and Technology Innovation High-end Talent Project of Jiangxi Province (jxsq2019201107), the International Science and Technology Cooperation of Jiangxi Province (20203BDH80W011) and the Graduate Students Innovation Special Foundation of Jiangxi Province (YC2021-B017).

Author contributions Peng Z conceived the idea of this study and wrote the manuscript. Peng Z, Guo J, He Q, and Li S conducted the experiments and analyzed the data. Chen Y and Tan L revised the paper and supervised the project. The paper was discussed through the contributions of all the authors.

Conflict of interest The authors declare that they have no conflict of interest.

Supplementary information Experimental details and supporting data are available in the online version of the paper.

Zhongyou Peng is a PhD candidate at the College of Chemistry and Chemical Engineering/Institute of Polymers and Energy Chemistry, Nanchang University. He received his BE degree from Nanchang University in 2018. His current research interests include the synthesis and characterization of nanomaterials for supercapacitors, planar supercapacitors, and hybrid ion capacitors.

Licheng Tan received her PhD degree from Nanchang University in 2012 under the supervision of Professor Yiwang Chen. In 2011, she joined Professor Andreas Greiner's group at the University of Marburg in Germany for cooperation research. She is currently a professor at Nanchang University. She was awarded as a National Excellent Young Scholar. Her current scientific interests include perovskite solar cells, polymer solar cells, and supercapacitors.

Yiwang Chen is a full professor of chemistry at Nanchang University and Jiangxi Normal University. He received his PhD degree from Peking University in 1999 and conducted his postdoctoral work at Johannes Gutenberg-Universität Mainz and Philipps-Universität Marburg in Germany, being awarded an Alexander von Humboldt fellowship. He joined Nanchang University in 2004. He was honored by the National Science Fund for Distinguished Young Scholars in 2014. He has been serving as vice president of Jiangxi Normal University since 2019, and as director of the Institute of Polymers and Energy Chemistry at Nanchang University since 2004. He was the dean of the College of Chemistry at Nanchang University in 2009–2019. His research interests include polymer solar cells, perovskite solar cells, supercapacitors, electrocatalysis for zinc-air batteries, and intelligent elastomer.

具有双离子吸附的多级结构氮掺杂碳球助力超高倍率及稳定的锌离子超级电容器

彭钟有[1], 郭俊晞[3], 何其昌[1], 李舒龙[1], 谈利承[1*], 陈义旺[1,2*]

摘要 尽管高能量水系锌离子超级电容器(ZHSCs)的研究取得了重要的进展, 但缓慢的锌离子扩散及不理想的阴极材料仍然限制了其能量密度和循环寿命. 在本文中, 我们设计了具有合适的孔径分布及优异的锌离子储存能力的氮掺杂分级碳球(NMCSs). 组装的ZHSCs在0.2 A g^{-1}的电流密度下, 表现出优异的电容量(157.8 mA h g^{-1})及能量密度(126.2 W h kg^{-1}), 具有卓越的功率密度(39.9 kW kg^{-1}). 此外, ZHSCs表现出了超长的循环稳定性, 在50,000次循环测试后仍能保持96.2%的初始电容量. 此外, 我们设计了一种新型的平面ZHSCs, 表现出优异的低温电化学性能, 超高的体积能量密度(31.6 mW h cm^{-3})和极佳的集成性能. 通过原位/非原位表征, 系统地揭示了NMCSs电极优异的电化学性能主要来源于阳离子和阴离子的协同吸附以及NMCSs的可逆化学吸附作用机理. 本工作不仅为新型高性能ZHSCs的构建和开发提供了新思路, 也为进一步理解ZHSCs的电化学储能机理提供了依据.

